

# Superionic Surface Li-Ion Transport in Carbonaceous Materials

Jianbin Zhou, Shen Wang, Chaoshan Wu, Ji Qi, Hongli Wan, Shen Lai, Tsz Wai Ko, Zhaohui Liang, Shijie Feng, Ke Zhou, Nimrod Harpak, Mengchen Liu, Zeyu Hui, Paulina J. Ai, Haodong Liu, Wenlin Yan, Yang Ha, Min-Jae Kim, Kent Griffith, Chunsheng Wang,\* Shyue Ping Ong,\* Yan Yao,\* and Ping Liu\*



Cite This: <https://doi.org/10.1021/acs.nanolett.5c02729>



Read Online

ACCESS |

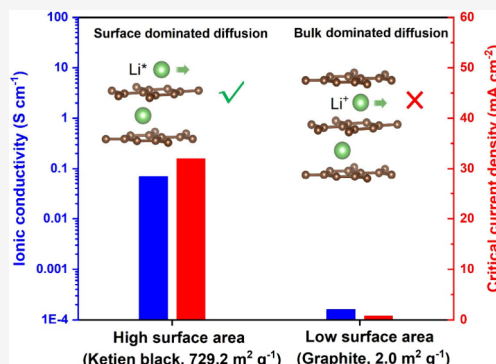
Metrics & More

Article Recommendations

Supporting Information

**ABSTRACT:** Unlike Li-ion transport in the bulk of carbonaceous materials, little is known about Li-ion diffusion on their surface. In this study, we have discovered an ultrafast Li-ion transport phenomenon on the surface of carbonaceous materials with limited reversible Li insertion capacity and high surface area. An ionic conductivity of  $18.1 \text{ mS cm}^{-1}$  at room temperature is observed in lithiated Ketjen black (KB), far exceeding those of most solid-state ion conductors. Theoretical calculations reveal low diffusion barriers for the surface Li species. As a result, lithiated KB functions effectively as an interlayer between Li and solid-state electrolytes (SSEs) to mitigate dendrite growth. Further, lithiated KB acts as a high-performance mixed ionic–electronic conductor and replaces solid electrolytes to enhance graphite anode performance, demonstrating full utilization with  $\sim 85\%$  capacity retention over 300 cycles. The discovery of this surface-mediated ultrafast Li-ion transport mechanism provides new directions for the design of solid-state ion conductors and solid-state batteries.

**KEYWORDS:** surface Li-ion transportation, carbonaceous materials, solid-state batteries, Li metal batteries



**L**i-ion transport in carbonaceous materials is an important process, underpinning their applications in rechargeable batteries.<sup>1–4</sup> Up to now, our understanding of this transport process is associated with the Li-ion diffusion in Li–C intercalation compounds.<sup>5,6</sup> The kinetics of such processes are highly dependent on the structures of the carbon materials, which can be categorized into three different types: graphite, hard carbon, and soft carbon.<sup>7,8</sup>

Li-ion transport in graphite, which consists of highly ordered, stacked graphene layers, is slow due to the high intercalation/diffusion barriers between the layers.<sup>9,10</sup> In contrast, hard carbons feature short-range graphitized domains, expanded interlayer distance, abundant voids or pores, and rich edges and defects.<sup>11</sup> These characteristics have endowed hard carbons with the ability to uptake Li-ion in nanopores and absorb Li-ions at defect sites, thus enabling fast intercalation/deintercalation.<sup>12,13</sup> Soft carbons have well-ordered graphene layers but with randomly stacked turbostratic structures,<sup>14</sup> which facilitates lithiation/delithiation.<sup>15,16</sup> Regardless of their structures, these bulk diffusion processes are generally slow. As a result, additional ion conductors, either liquid or solid, are needed to enable these carbon materials to function as electrode materials with reasonable rates.<sup>17,18</sup>

In contrast, the transport of Li on the surface of carbon is virtually unexplored due to two factors. Carbonaceous materials used in batteries tend to have very low surface

area, which is necessary to reduce the parasitic reactions and the amount of charge consumed to form the solid electrolyte interphase (SEI) in organic electrolytes.<sup>3,19</sup> In addition, the presence of the SEI also makes the observation of any surface transport processes unfeasible.<sup>20–22</sup> However, understanding the transport of Li on the surface of carbon is important both scientifically and technologically. Scientifically, the chemical state of the Li-ion on the surface can be significantly different from the bulk, which might be essential for fast transport. Technologically, realizing rapid Li-ion transport on the carbon surface enables a variety of applications. In addition to being a high-rate electrode material,<sup>23,24</sup> carbon has also been used as an interlayer to protect Li metal electrodes in solid-state batteries by guiding Li deposition away from the SSE interface.<sup>25–27</sup> However, Li-intercalated carbon is usually lithophilic.<sup>28</sup> Consequently, a carbon interlayer needs to have limited Li intercalation capacity but offers a fast transport of Li. Finally, there is a pressing need to develop a mixed ion and electron conductor (MIEC) that is thermodynamically

Received: May 21, 2025

Revised: August 11, 2025

Accepted: August 12, 2025



ACS Publications

© XXXX American Chemical Society

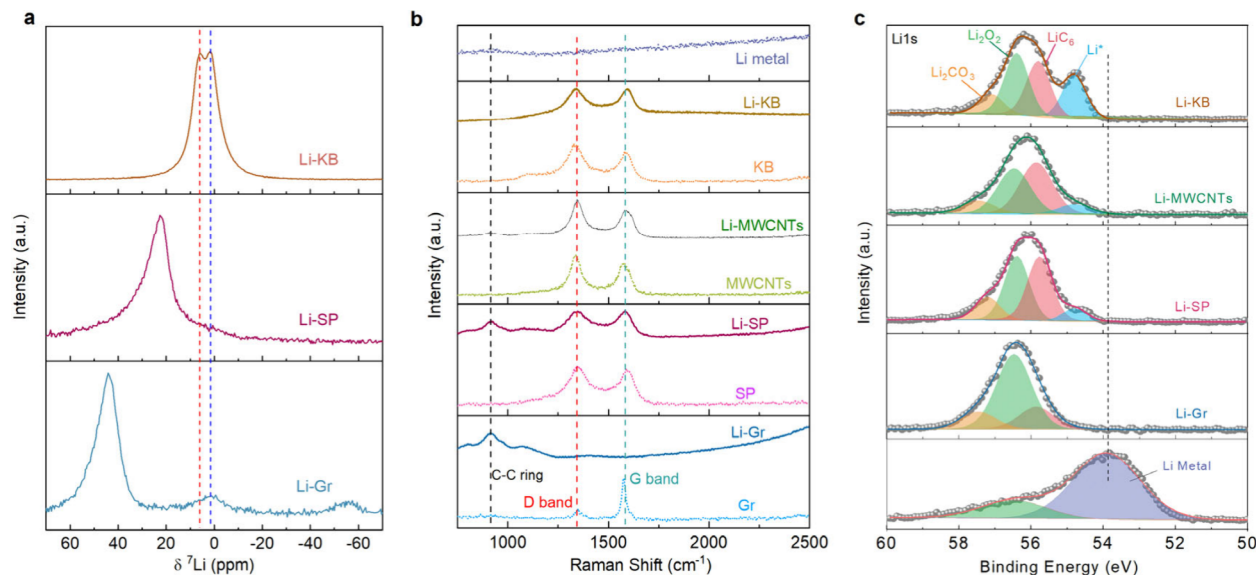


**Figure 1.** (a)  ${}^7\text{Li}$  NMR spectra of Li-Gr, Li-SP, and Li-KB; (b) Raman spectra of KB, MWCNTs, SP, and Gr before and after lithiation; and (c) high-resolution Li 1s XPS of Li-KB, Li-MWCNTs, Li-SP, Li-Gr and Li metal.

stable near the potential of Li metal to enable high-rate, long-life anodes for solid-state batteries. A notable advancement is a porous MIEC based on a garnet structure that has shown significant potential of enabling stable cycling of Li metal at high current densities and capacities.<sup>29</sup>

Solid-state batteries provide a unique platform to study the Li-ion transport on the surface of carbon in light of the absence of an SEI layer. In this regard, we have systematically studied the surface structures of lithiated carbonaceous materials with a variety of structures and surface area values. We have identified a partially charged  $\text{Li}^*$  species on the surface of lithiated carbon black materials. Theoretical calculations reveal a diffusion barrier of  $\text{Li}^*$  on the surface of lithiated carbon as low as 0.149 eV and approximately one-third of the value in the bulk structure. Consequently, an effective ionic conductivity of  $18.1 \text{ mS cm}^{-1}$  at room temperature is observed. The rapid surface  $\text{Li}^*$  transport mechanism enables lithiated carbon blacks with large surface area values to serve as effective interlayers between Li metal and an SSE layer, and an MIEC to enable a stable graphite anode. The discovery of this surface-mediated ultrafast Li transportation mechanism provides new directions for the materials design of solid ion conductors and solid-state batteries.

To study the reaction between Li and carbon, we selected six carbon materials with different structures and surface area values (details in Table S1 and Figure S1): graphite (Gr,  $2.0 \text{ m}^2 \text{ g}^{-1}$ ), mesocarbon microbead synthetic graphite (MCMB,  $2.2 \text{ m}^2 \text{ g}^{-1}$ ), carbon black (CB,  $29.1 \text{ m}^2 \text{ g}^{-1}$ ), Super-P (SP,  $57.5 \text{ m}^2 \text{ g}^{-1}$ ), multiwall carbon nanotubes (MWCNTs,  $208.3 \text{ m}^2 \text{ g}^{-1}$ ), and Ketjen black (KB,  $729.2 \text{ m}^2 \text{ g}^{-1}$ ). Their lithiated forms are labeled as Li-Gr, Li-MCMB, Li-SP, Li-MWCNTs, and Li-KB, respectively. We note that both the surface area and crystal structure might influence our findings. However, as shown later, surface area has a dominant influence on Li-ion conductivity, while crystal structure mainly impacts intercalation capacities. Further, a single material, such as MWCNTs, with different surface areas would make a good candidate for our study. However, the lack of tunability of the surface area in a large range makes it less ideal. Finally, studying Li transport through a single MWCNT would yield significant physical

insights but would require high precision microfabrication platforms.

To reveal the chemical environment of Li, Li-Gr, Li-SP, and Li-KB are investigated by solid-state nuclear magnetic resonance spectroscopy (NMR, Figure 1a). Li-Gr shows a single peak at 43 ppm, which is the typical peak assigned to  $\text{LiC}_6$ .<sup>30</sup> In contrast, Li-SP shows one peak at 22.3 ppm, while Li-KB has two peaks at 6.5 and 1.3 ppm, respectively. Temperature-dependent NMR experiments (Figure S2 and Figure S3a–3d) feature a much higher Li-ion mobility at 6.5 ppm with a reduced fwhm and shorter  $T_1$  relaxation time upon the increase of temperature,<sup>31</sup> while the peak at 1.3 ppm has negligible temperature sensitivity. A  ${}^7\text{Li}-{}^7\text{Li}$  2D-EXSY experiment (Figure S3e) shows the two peaks in Li-KB do not have apparent exchange, indicative of two different Li chemical environments.

To further resolve the chemical environment of Li, we turn to Raman and X-ray photoelectron (XPS) spectroscopy. The Raman spectra show that these carbons exhibit very different reactivity toward Li (Figure 1b). Gr shows a disappearance of its D and G bands upon lithiation, while a new peak close to  $900 \text{ cm}^{-1}$  arises, which is attributed to the C–C ring breathing mode.<sup>32</sup> Additional weak peaks arising near  $1100 \text{ cm}^{-1}$  can be indexed to the C–O bond in  $\text{Li}_2\text{CO}_3$ .<sup>33</sup> Li-SP exhibits a slight intensity decrease in its D and G bands, while Li-MWCNTs display an even smaller change in their D and G bands. Li-KB, in contrast, does not show any change in spectra as compared to pristine KB. The Raman spectra indicate that the bulk reactivity follows the order Gr > SP > MWCNTs > KB, which is consistent with their reversible intercalation capacities (Figure S4a,b).<sup>17</sup>

The peaks in survey XPS spectra for all samples (Figure S4c) can be resolved by referring to previous studies.<sup>34</sup> A new peak at 54.8 eV is observed in the spectra of Li-KB, Li-SP, and Li-MWCNTs (Figure 1c). This peak has a higher binding energy than Li metal (at 53.8 eV) but lower than  $\text{LiC}_6$ , suggesting a special  $\text{Li}^*$  species that has not been observed before. Among all the samples, Li-KB has the highest ratio of  $\text{Li}^*$ . Again, this carbon has the highest surface area and the lowest reversible intercalation capacity as well. On the contrary, this peak is not

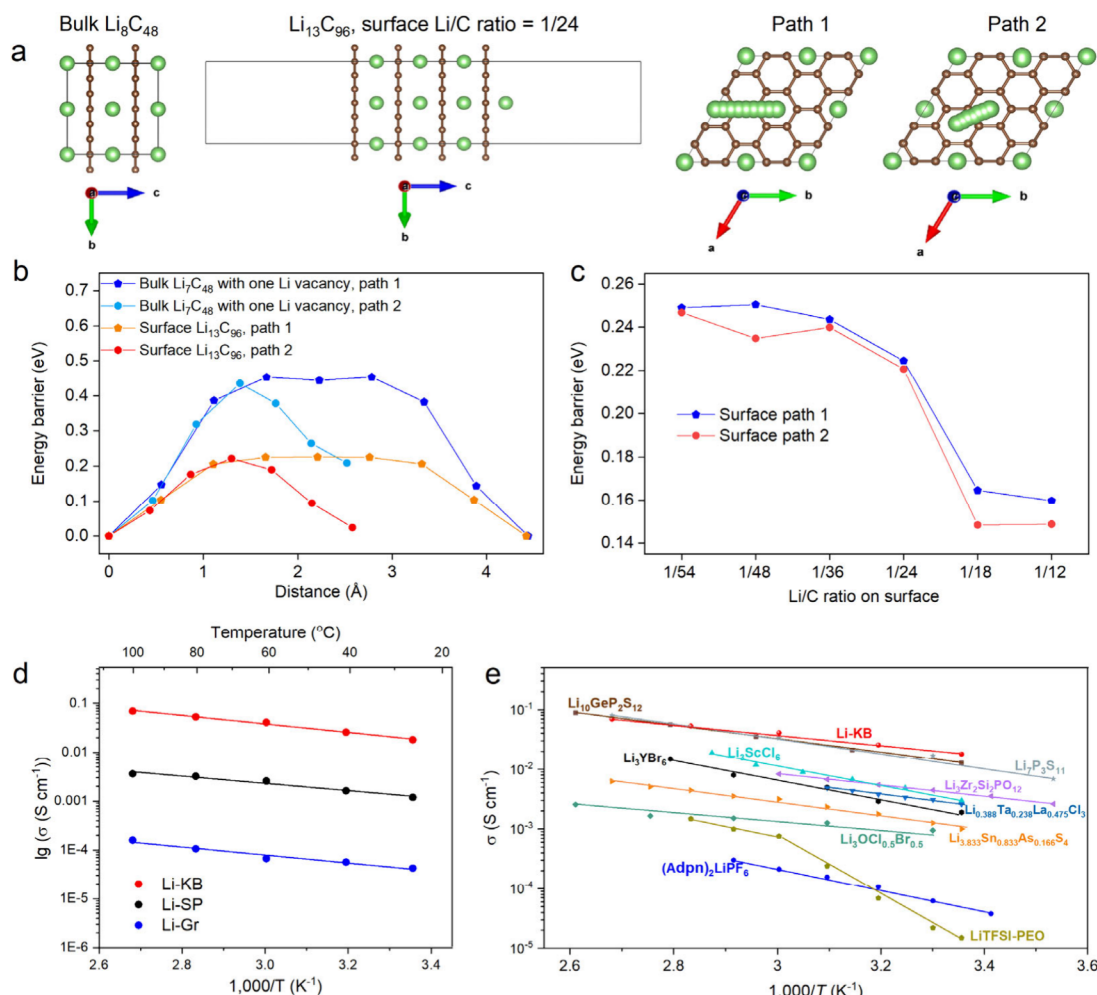


**Figure 2.** (a) Bulk and surface structures of lithiated carbon and two migration pathways of  $\text{Li}^*$ . (b) CI-NEB energy landscapes for the two types of  $\text{Li}^*$  migration paths in bulk  $\text{Li}_7\text{C}_{48}$  with one Li vacancy and on the surface of  $\text{Li}_{13}\text{C}_{96}$  with a surface Li/C ratio of 1/24. (c) CI-NEB  $\text{Li}^*$  migration energy barriers with respect to Li/C ratios on the surface of lithiated carbon. (d) The ionic conductivities of Li-Gr, Li-SP, and Li-KB at different temperatures. (e) Ionic conductivity comparison between Li-KB and other solid-state ionic conductors.

observed in Gr. Electron energy loss spectra (EELS) of Li-Gr and Li-KB measured by using cryo-TEM further confirm the existence of  $\text{Li}^*$  on the surface of the carbon materials (Figure S5 and Supporting Information Note 1).

Climbing image nudged elastic band (CI-NEB) simulations<sup>35</sup> were conducted to determine the  $\text{Li}^*$  migration barriers on the surface and in the bulk of lithiated carbon. A  $2 \times 2 \times 2$  supercell of bulk  $\text{LiC}_6$  with one Li vacancy and  $n_a \times n_b \times 4$  slab supercells of  $\text{LiC}_6$  with one  $\text{Li}^*$  on the surface were used (Figure 2a), where  $n_a$  and  $n_b$  are the integer multiples of the  $a$  and  $b$  lattice parameters. The migration barriers of Li in the bulk are 0.436–0.453 eV, in line with previous studies.<sup>36,37</sup> In contrast, the  $\text{Li}^*$  diffusion barriers on the surface of  $\text{Li}_{13}\text{C}_{96}$  (surface Li/C = 1/24) are 0.222–0.226 eV, almost half of that in the bulk. With the Li/C ratio increasing from 1/54 to 1/12, the  $\text{Li}^*$  migration barriers decrease (Figure 2c). At a surface Li/C ratio of 1/12, the  $\text{Li}^*$  migration barriers are 0.149–0.160 eV, lower than well-known Li superionic conductors (e.g.,  $\text{Li}_{10}\text{GeP}_2\text{S}_{12}$  with a diffusion activation barrier of 0.21–0.24 eV).<sup>38,39</sup> Even in the presence of defects, Li diffusion on lithiated carbon surfaces is still far more facile than in bulk (Figures S6–8, Table S2, and Supporting Information Note 2). Overall, CI-NEB simulations indicate significantly more facile

$\text{Li}^*$  migration on the surface than in the bulk of lithiated carbon.

To directly measure the ionic conductivities of different carbon materials, we constructed a symmetric cell with a structure of Li/C/LPSCL/C/Li. Based on the resistance differences with different C layer thicknesses (Figures S9–11 and Table S3) as determined by a direct current (DC) method, the ionic resistance of carbon interlayers can be calculated, which is in turn used to estimate their ionic conductivities. The DC method is more appropriate than the electrochemical impedance method due to their high electronic conductivity.<sup>40</sup> More details are shown in the Methods. As shown Figure 2d, Li-KB has Li ionic conductivity values of 18.1, 25.8, 41.1, 53.2, and 69.6  $\text{mS cm}^{-1}$  at 25, 40, 60, 80, and 100 °C, respectively. The activation energy for  $\text{Li}^*$  migration in Li-KB is calculated to be 0.17 eV, matching well with the results predicated by CI-NEB. Moreover, the ionic conductivities of Li-KB are 10× higher than those of Li-SP and almost 10<sup>3</sup>× higher than those of Li-Gr at the same temperature, consistent with our hypothesis that surface Li transport plays a dominant role. Li-KB exhibits the highest ionic conductivity at room temperature compared to other solid-state Li-ion conductors (Figure 2e).

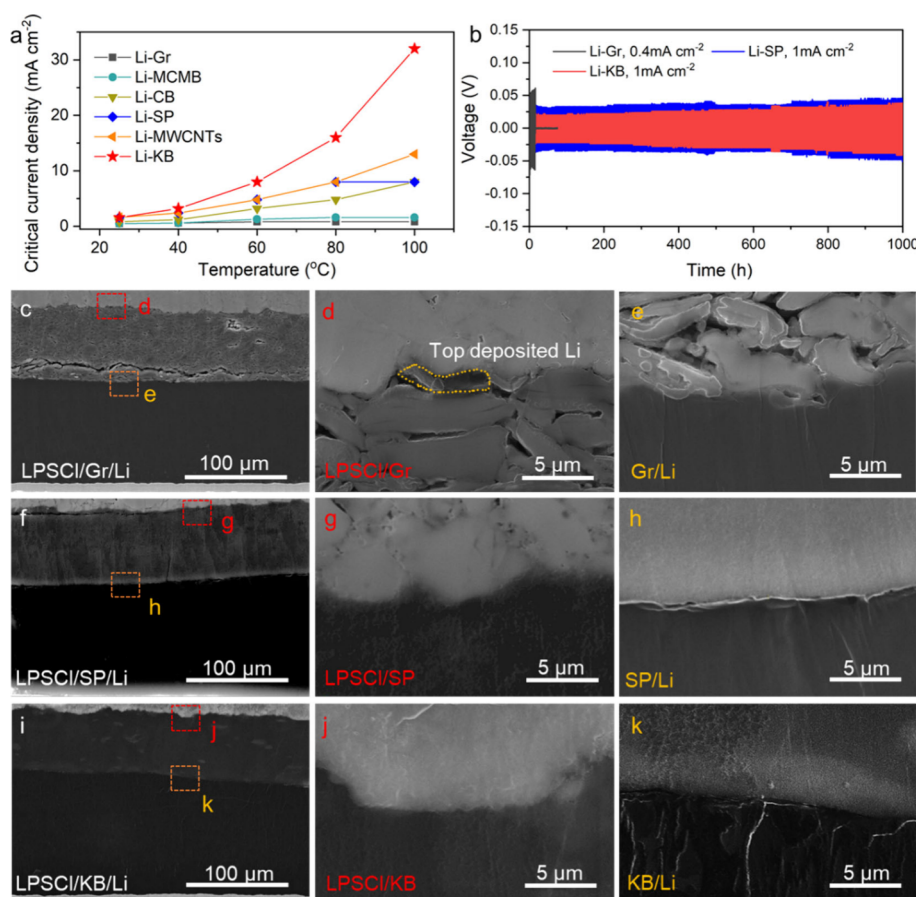


**Figure 3.** (a) CCDs of carbon interlayers in the Li/C/LPSCl/C/Li symmetric cells. (b) The cycling performance of the KB interlayer at 1.0  $\text{mA cm}^{-2}$ , SP interlayer at 1.0  $\text{mA cm}^{-2}$ , and Gr interlayer at 0.4  $\text{mA cm}^{-2}$ . Cross-sectional SEM images of Li/C/LPSCl interfaces after plating Li metal with different C: (c–e) Gr, 2.0  $\text{mAh cm}^{-2}$ , 0.2  $\text{mA cm}^{-2}$ ; (f–h) SP, 5.0  $\text{mAh cm}^{-2}$ , 1.0  $\text{mA cm}^{-2}$ ; (i–k) KB, 5.0  $\text{mAh cm}^{-2}$ , 1.0  $\text{mA cm}^{-2}$ .

To explore the functions of ultrafast surface Li\* transport on carbon, we first use them as interlayers to circumvent the challenges of the Li metal anode. Li/C/LPSCl/C/Li symmetric cells are constructed to measure the critical current densities (CCDs). As an example, the CCDs of cells with KB interlayers are measured with stepwise increase in current densities (from 0.1 to 50  $\text{mA cm}^{-2}$ ). As shown in Figure S12, with increasing temperature from 25 to 100  $^{\circ}\text{C}$ , the CCDs of KB interlayers increase dramatically from 2.4 to 32.0  $\text{mA cm}^{-2}$ . The CCDs of the other 5 different carbon interlayers (Figures S13–17) are summarized in Figure 3a. At the same temperature, there is an apparent positive correlation between the surface area and CCDs. High surface area carbon has a prominent surface transport mechanism with limited Li insertion into its bulk. For each carbon, CCDs increase with temperature, which is associated with the ionic conductivity of the interlayers. The CCD values delivered by Li-KB are among the highest values of interlayers reported so far (Figure S18 and Table S4), which can be further improved by designing a porous MIEC host structure for Li.<sup>29</sup>

The cycling stability of Li/C/LPSCl/C/Li symmetric cells is also evaluated at 60  $^{\circ}\text{C}$ . At a current density of 1.0  $\text{mA cm}^{-2}$ , cells with KB and SP interlayers (Figure 3b) cycle stably over 1000 h without short circuiting. In contrast, the Gr interlayer-based symmetric cell is shorted even at 0.4  $\text{mA cm}^{-2}$  after cycling for 16 h. Moreover, the KB interlayer-based symmetric cell cycled at 60  $^{\circ}\text{C}$  exhibits a negligible increase in impedance over 1000 h (Figure S19).

To visualize the deposition behavior of Li, we captured cross-sectional SEM images of the Li/C/LPSCl/C/Li cells after plating/stripping the Li metal (Figure 3c–k). The images of the cell with Gr interlayers after undergoing 10 h of cycling at 0.2  $\text{mA cm}^{-2}$  and 40  $^{\circ}\text{C}$  (Figure S20a) are displayed in Figure 3c–e and Figures S21 and 22. We observe a small amount of Li deposited between LPSCl and Gr. This deposition likely serves as a starting point to induce more deposition at this interface, leading to Li dendrite formation and short circuiting. SEM images of a symmetric cell with an SP interlayer are shown in Figure 3f–h and Figures S23 and S24. The cell underwent 5.0  $\text{mAh cm}^{-2}$  of cycling at 1.0  $\text{mA cm}^{-2}$  (Figure S20b) and 40  $^{\circ}\text{C}$ . The images reveal that the SP interlayers maintain excellent contact with LPSCl and Li on both sides. The SP interlayer successfully prevented the formation of Li dendrites. All of the Li is plated underneath the SP interlayer. The Li layers are very dense: there is a thickness difference of ~50  $\mu\text{m}$  between the two sides (Figures S23a and 24a), matching well with the expected Li thickness difference (~50  $\mu\text{m}$  for moving 5  $\text{mAh cm}^{-2}$ ). Similar results are obtained with KB interlayers in symmetric cells as shown in Figure 3i–k and Figures S25 and S26, which were cycled at 40  $^{\circ}\text{C}$  for 5 h at 1  $\text{mA cm}^{-2}$  (Figure S20c). In cells with SP or KB interlayers, Li appears to go through the carbon interlayers and uniformly deposits or strips at the Li/interlayer interface. Such a phenomenon is attributed to the high ionic conductivity of the carbon. Despite the fact that carbon is electronically conductive, the differences in Li nucleation on carbon versus

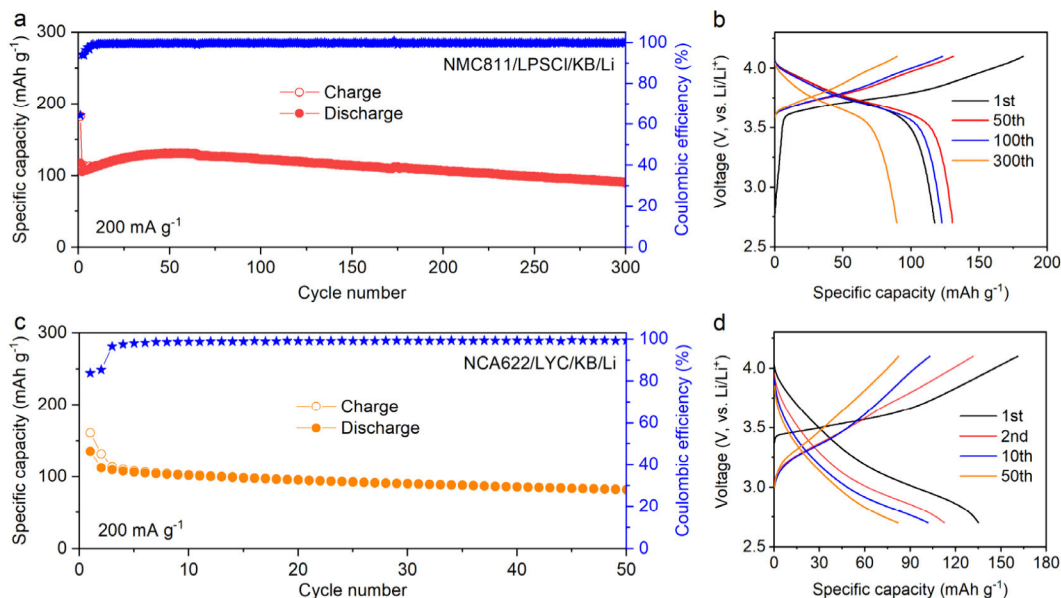


**Figure 4.** (a) NMC811/LPSCI/KB@MWCNTs/Li cell cycling performance at 60 °C and at 200 mA g<sup>-1</sup> and (b) the corresponding voltage profiles. (c) NCA622/LYC/KB@MWCNTs/Li cell cycling performance at 60 °C and at 200 mA g<sup>-1</sup> and (d) the corresponding voltage profiles.

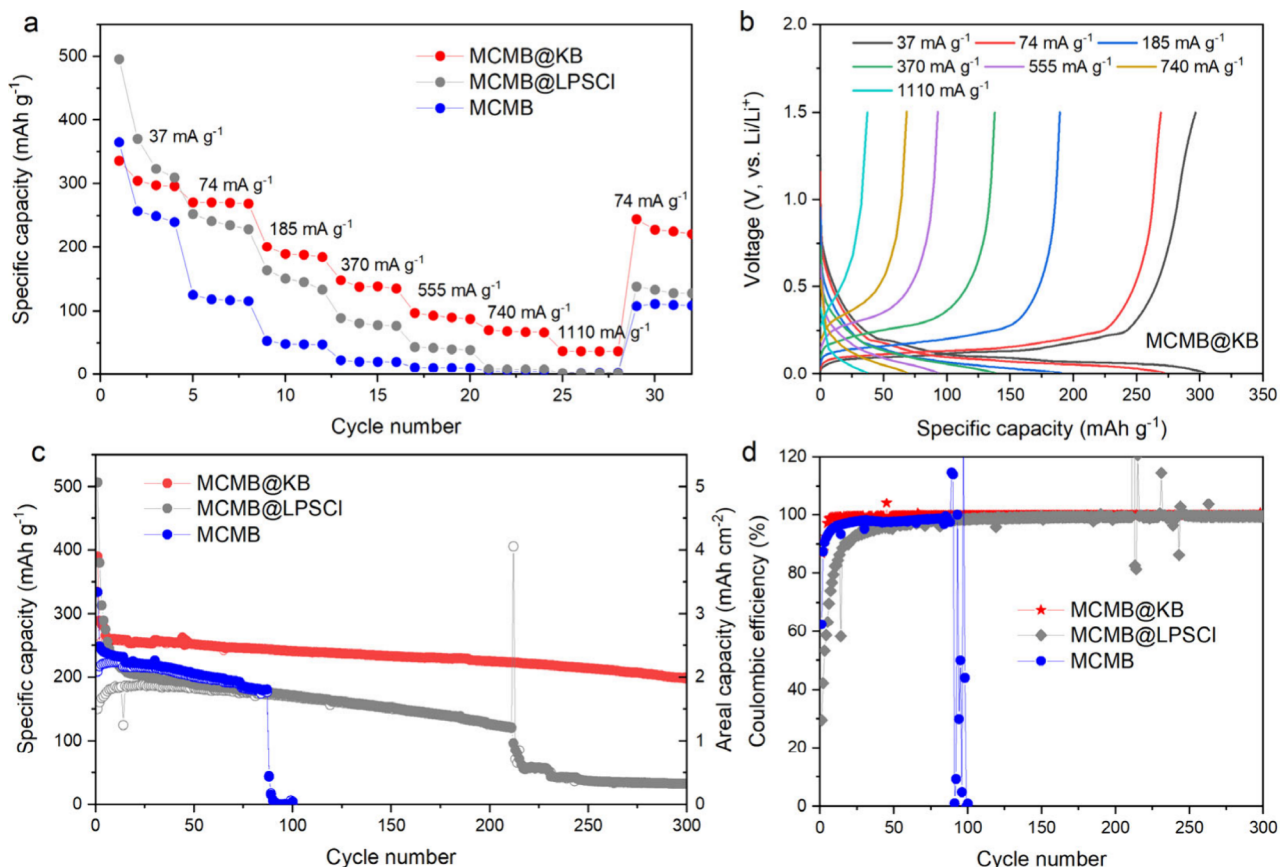


**Figure 5.** (a) Rate performance of pure MCMB, MCMB@KB, and MCMB@LPSCI at current densities from 37 to 1110 mA g<sup>-1</sup> and at 60 °C. (b) Corresponding voltage profiles of the MCMB@KB anode at different rates. (c) The cycling performance of pure MCMB, MCMB@KB, and MCMB@LPSCI anodes at 74 mA g<sup>-1</sup> and at 60 °C in SSBs (initial cycle was tested at 37 mA g<sup>-1</sup>). (d) The corresponding Coulombic efficiencies in (c).

on Li are sufficient to drive preferential Li deposition at the carbon/Li interface. On the stripping side, the large surface area of carbon interlayers also contributes to mitigating void formation at the interface ([Supporting Information, Note 3](#)).

To further illustrate the relationship between CCD and Li deposition patterns, we also characterized the symmetric cells cycled above their CCDs ([Figures S27–31](#)). When the cell with the SP interlayers is cycled at 40 °C and 6 mA cm<sup>-2</sup>, there

is dendritic Li deposition occurring between the SP interlayer and LPSCl (Figure S28). On the stripping side, the LPSCl/SP interface is still well maintained, but the contact at the SP/Li interface is poor (Figure S29). In the cells with KB interlayers, it is the same with the SP interlayer (Figures S30 and S31). These findings show that when the transport resistance of Li through the interlayer is higher than the differences in nucleation energy, Li will deposit at the electrolyte/interlayer interface.

We have identified KB as a very promising material to provide rapid surface Li transport. Next, we evaluate its suitability as an interlayer material in SSBs to improve the Li metal anode stability. A self-standing KB@MWCNTs film is fabricated with a KB:MWCNTs weight ratio of 7:3 and a mass loading of  $1.5 \text{ mg cm}^{-2}$  (Figure S32a). The film thickness is  $\sim 11 \mu\text{m}$  (Figure S32b). When evaluated as an interlayer in a symmetric cell, the CCD is  $8.0 \text{ mA cm}^{-2}$  at  $60^\circ\text{C}$  (Figure S32c), which is the same with the pure KB interlayer. We note that MWCNTs here mainly improve the mechanical integrity of the freestanding interlayer with negligible contribution to Li transport, as evidenced by the CCD value. A full cell with a structure of NMC811/LPSCl/KB@MWCNTs/Li is fabricated. As shown in Figure 4a,b, the cell achieves a capacity retention of  $\sim 85\%$  after 300 cycles at a rate of  $200 \text{ mA g}^{-1}$ . In contrast, the cell without the interlayer is short-circuited in the first cycle at a current density of  $100 \text{ mA g}^{-1}$  (Figure S33a). Even at a lower rate of  $20 \text{ mA g}^{-1}$ , the cell without the interlayer is also short-circuited by the 21st cycle (Figure S33b).

In principle, the ability of the carbon interlayer to suppress Li dendrite growth is agnostic to the electrolyte material. In this regard, we also fabricated both symmetric and full cells by replacing LPSCl with  $\text{Li}_3\text{YCl}_6$  (LYC). As expected, the symmetric cell cycled stably for over 1000 h at  $0.2 \text{ mA cm}^{-2}$  (Figure S34). A full cell can be cycled at a rate of  $200 \text{ mA g}^{-1}$  for 50 cycles without a short circuit (Figure 4c,d). In contrast, the control cell without the interlayer is short-circuited at the fifth cycle even at  $50 \text{ mA g}^{-1}$  (Figure S33c). The ability of the interlayer to protect Li by enabling preferential deposition at the interlayer/Li interface is very encouraging.<sup>50</sup>

KB is further explored as a thermodynamically stable MIEC to enable stable anodes in SSBs. Here, MCMB is evaluated as an anode material for an SSB cell. Instead of adding a solid electrolyte into the anode composite, we added Li-KB. Previously, sulfide SSE has been shown to suffer from significant decomposition at low working potentials.<sup>17</sup> MCMB, with or without added KB, is directly pressed on a piece of Li metal. As shown in Figure 5a, an MCMB electrode with 10 wt % of pre lithiated KB displays much higher rate capabilities than pure MCMB or MCMB mixed with LPSCl electrodes in MCMB/LPSCl/KB/Li half-cells. It should be noted that the mass loading of MCMB is  $\sim 10 \text{ mg cm}^{-2}$ . The cells are tested at rates from 37 to  $1110 \text{ mA g}^{-1}$  at  $60^\circ\text{C}$ . The voltage profiles of the MCMB@KB anode show the signature voltage plateaus for graphite (Figure 5b), indicating the much more favorable electrode kinetics compared to the other two electrodes (Figure S35a,b). The long-term cycling stabilities of the three carbon anodes are measured at  $74 \text{ mA g}^{-1}$  and at  $60^\circ\text{C}$  (Figure 5c). The MCMB@KB anode shows a capacity retention of  $\sim 85\%$  after 300 cycles with an average Coulombic efficiency of over 99.6%. In contrast, the MCMB and MCMB@LPSCl electrodes suffer from shorting at the 87th and 212th cycle, respectively. Further, MCMB@LPSCl shows

much lower Coulombic efficiency than MCMB@KB (Figure 5d). Therefore, KB is a thermodynamically stable, high-conductivity material that is well-suited for high-performance SSB anodes. It should be noted that pre lithiation is necessary for KB (Figure S36 and Supporting Information Note 2). Pre lithiation compensates for the irreversible loss of Li due to trapping in hard carbon materials and provides the necessary Li concentration to achieve high ionic conductivity. Further, the Li metal layer also effectively serves as the surface to facilitate Li deposition.

In summary, we have discovered a new surface-mediated Li-ion transport mechanism in carbon materials. For carbon blacks with a high surface area and low intercalation capacity, lithiation enables materials with high ionic conductivities and low migration barriers. These carbon materials have shown great potential in SSBs either as interlayers to protect the Li metal anode or as a thermodynamically stable MIEC for constructing other anodes (e.g., MCMB). The discovery of this surface-mediated ultrafast Li-ion transportation mechanism provides a new direction for the design of other solid-state ionic conductors. Our work advocates for a set of design rules for these materials: high surface area, thermodynamic stability at the potential of operation, and a weak interaction between the ion and the surface. We also expect such a mechanism to be applicable for other alkaline ions, as well.

## ■ ASSOCIATED CONTENT

### SI Supporting Information

The Supporting Information is available free of charge at <https://pubs.acs.org/doi/10.1021/acs.nanolett.5c02729>.

The materials preparation processes, cell fabrications, test details, characterizations, DFT calculations, SEM, EDS mapping images, NMR, BET curves, CCD tests, EELS, symmetric cell tests ([PDF](#))

## ■ AUTHOR INFORMATION

### Corresponding Authors

Chunsheng Wang — Department of Chemical and Biomolecular Engineering, University of Maryland, College Park, Maryland 20742, United States;  [orcid.org/0000-0002-8626-6381](https://orcid.org/0000-0002-8626-6381); Email: [cswang@umd.edu](mailto:cswang@umd.edu)

Shyue Ping Ong — Aiiso Yufeng Li Family Department of Chemical and Nano Engineering, University of California, San Diego, La Jolla, California 92093, United States;  [orcid.org/0000-0001-5726-2587](https://orcid.org/0000-0001-5726-2587); Email: [ongsp@ucsd.edu](mailto:ongsp@ucsd.edu)

Yan Yao — Materials Science and Engineering Program and Texas Center for Superconductivity at the University of Houston, University of Houston, Houston, Texas 77204, United States; Email: [yyao4@central.uh.edu](mailto:yyao4@central.uh.edu)

Ping Liu — Aiiso Yufeng Li Family Department of Chemical and Nano Engineering, University of California, San Diego, La Jolla, California 92093, United States;  [orcid.org/0000-0002-1488-1668](https://orcid.org/0000-0002-1488-1668); Email: [piliu@ucsd.edu](mailto:piliu@ucsd.edu)

### Authors

Jianbin Zhou — Aiiso Yufeng Li Family Department of Chemical and Nano Engineering, University of California, San Diego, La Jolla, California 92093, United States

Shen Wang — Aiiso Yufeng Li Family Department of Chemical and Nano Engineering, University of California, San Diego, La Jolla, California 92093, United States

**Chaoshan Wu** — Materials Science and Engineering Program and Texas Center for Superconductivity at the University of Houston, University of Houston, Houston, Texas 77204, United States

**Ji Qi** — Aiiso Yufeng Li Family Department of Chemical and Nano Engineering, University of California, San Diego, La Jolla, California 92093, United States;  [orcid.org/0000-0001-5808-9931](https://orcid.org/0000-0001-5808-9931)

**Hongli Wan** — Department of Chemical and Biomolecular Engineering, University of Maryland, College Park, Maryland 20742, United States

**Shen Lai** — Department of Chemistry and Biochemistry, University of California, San Diego, La Jolla, California 92093, United States

**Tsz Wai Ko** — Aiiso Yufeng Li Family Department of Chemical and Nano Engineering, University of California, San Diego, La Jolla, California 92093, United States

**Zhaohui Liang** — Aiiso Yufeng Li Family Department of Chemical and Nano Engineering, University of California, San Diego, La Jolla, California 92093, United States

**Shijie Feng** — Aiiso Yufeng Li Family Department of Chemical and Nano Engineering, University of California, San Diego, La Jolla, California 92093, United States;  [orcid.org/0000-0001-5797-8542](https://orcid.org/0000-0001-5797-8542)

**Ke Zhou** — Aiiso Yufeng Li Family Department of Chemical and Nano Engineering, University of California, San Diego, La Jolla, California 92093, United States

**Nimrod Harpak** — Aiiso Yufeng Li Family Department of Chemical and Nano Engineering, University of California, San Diego, La Jolla, California 92093, United States

**Mengchen Liu** — Aiiso Yufeng Li Family Department of Chemical and Nano Engineering, University of California, San Diego, La Jolla, California 92093, United States

**Zeyu Hui** — Aiiso Yufeng Li Family Department of Chemical and Nano Engineering, University of California, San Diego, La Jolla, California 92093, United States

**Paulina J. Ai** — The Bishop's School, La Jolla, California 92037, United States

**Haodong Liu** — Aiiso Yufeng Li Family Department of Chemical and Nano Engineering, University of California, San Diego, La Jolla, California 92093, United States

**Wenlin Yan** — Aiiso Yufeng Li Family Department of Chemical and Nano Engineering, University of California, San Diego, La Jolla, California 92093, United States

**Yang Ha** — Advanced Light Source, Lawrence Berkeley National Laboratory, Berkeley, California 94720, United States;  [orcid.org/0000-0001-5684-8420](https://orcid.org/0000-0001-5684-8420)

**Min-Jae Kim** — Advanced Light Source, Lawrence Berkeley National Laboratory, Berkeley, California 94720, United States

**Kent Griffith** — Department of Chemistry and Biochemistry, University of California, San Diego, La Jolla, California 92093, United States;  [orcid.org/0000-0002-8096-906X](https://orcid.org/0000-0002-8096-906X)

Complete contact information is available at:

<https://pubs.acs.org/10.1021/acs.nanolett.5c02729>

## Author Contributions

J.Z. and P.L. conceptualized the idea and designed all of the experiments. S.W. did the XPS and Raman tests and result analysis. Chaoshan Wu and Y.Y. collected the cross-sectional SEM and EDX mapping images. J.Q., T.W.K., and S.P.O. performed the theoretical calculations. H.W. and Chunsheng

Wang tested the full cell performance. S.L. and K.G. performed the NMR measurement. N.H., S.F., Z.L., H.L., N.S., C.S., Z.H., P.A., W.Y., Y.H., and M.J. helped with the materials preparation, characterizations, result analysis, and manuscript revision. J.Z. and P.L. drafted the manuscript with the input and revision from all authors. Chunsheng Wang, S.P.O., Y.Y., and P.L. supervised this research. J.Z., S.W., Chaoshan Wu, J.Q., and H.W. contributed equally to this work.

## Notes

The authors declare no competing financial interest.

## ACKNOWLEDGMENTS

This work is supported by the Advanced Research Projects Agency-Energy, U.S. Department of Energy (DOE), under Contract No. DE-AR0000781.

## REFERENCES

- (1) Fong, R.; Von Sacken, U.; Dahn, J. R. Studies of lithium intercalation into carbons using nonaqueous electrochemical cells. *J. Electrochem. Soc.* **1990**, *137* (7), 2009–2013.
- (2) Manthiram, A. An Outlook on Lithium Ion Battery Technology. *ACS Cent. Sci.* **2017**, *3* (10), 1063–1069.
- (3) Xu, K. Electrolytes and interphases in Li-ion batteries and beyond. *Chem. Rev.* **2014**, *114* (23), 11503–11618.
- (4) Roberts, A. D.; Li, X.; Zhang, H. Porous carbon spheres and monoliths: morphology control, pore size tuning and their applications as Li-ion battery anode materials. *Chem. Soc. Rev.* **2014**, *43* (13), 4341–4356.
- (5) Xie, L.; Tang, C.; Bi, Z.; Song, M.; Fan, Y.; Yan, C.; Li, X.; Su, F.; Zhang, Q.; Chen, C. Hard Carbon Anodes for Next-Generation Li-Ion Batteries: Review and Perspective. *Adv. Energy Mater.* **2021**, *11* (38), No. 2101650.
- (6) Kaskhedikar, N. A.; Maier, J. Lithium Storage in Carbon Nanostructures. *Adv. Mater.* **2009**, *21* (25–26), 2664–2680.
- (7) Adams, R. A.; Varma, A.; Pol, V. G. Carbon Anodes for Nonaqueous Alkali Metal-Ion Batteries and Their Thermal Safety Aspects. *Adv. Energy Mater.* **2019**, *9* (35), No. 1900550.
- (8) Cao, W. J.; Zheng, J. S.; Adams, D.; Zheng, J. P. Comparative Study of the Power Performance for Advanced Li-Ion Capacitors with Various Carbon Anodes. *ECS Trans.* **2014**, *61* (18), 37.
- (9) Yu, P.; Popov, B. N.; Ritter, J. A.; White, R. E. Determination of the Lithium Ion Diffusion Coefficient in Graphite. *J. Electrochem. Soc.* **1999**, *146* (1), 8.
- (10) Xie, J.; Lu, Y. C. A retrospective on lithium-ion batteries. *Nat. Commun.* **2020**, *11* (1), 2499.
- (11) Saurel, D.; Segalini, J.; Jauregui, M.; Pendashteh, A.; Daffos, B.; Simon, P.; Casas-Cabanas, M. A SAXS outlook on disordered carbonaceous materials for electrochemical energy storage. *Energy Storage Mater.* **2019**, *21*, 162–173.
- (12) Li, Q.; Zhang, J.; Zhong, L.; Geng, F.; Tao, Y.; Geng, C.; Li, S.; Hu, B.; Yang, Q. Unraveling the Key Atomic Interactions in Determining the Varying Li/Na/K Storage Mechanism of Hard Carbon Anodes. *Adv. Energy Mater.* **2022**, *12* (37), No. 2201734.
- (13) Dahn, E. B.; Dahn, J. R. Li-insertion in hard carbon anode materials for Li-ion batteries. *Electrochim. Acta* **1999**, *45* (1–2), 121–130.
- (14) Yu, K.; Liu, C.; Wang, Y.; Zheng, H.; Li, H.; Zhang, X.; Bai, H.; Ma, T.; Qiu, J. Molecular tuning of sulfur doped quinoline oligomer derived soft carbon for superior potassium storage. *Carbon* **2022**, *191*, 10–18.
- (15) Jian, Z.; Bommier, C.; Luo, L.; Li, Z.; Wang, W.; Wang, C.; Greaney, P. A.; Ji, X. Insights on the Mechanism of Na-Ion Storage in Soft Carbon Anode. *Chem. Mater.* **2017**, *29* (5), 2314–2320.
- (16) Chen, Z.; Wang, Q.; Amine, K. Improving the performance of soft carbon for lithium-ion batteries. *Electrochim. Acta* **2006**, *51* (19), 3890–3894.

- (17) Xing, X.; Li, Y.; Wang, S.; Liu, H.; Wu, Z.; Yu, S.; Holoubek, J.; Zhou, H.; Liu, P. Graphite-Based Lithium-Free 3D Hybrid Anodes for High Energy Density All-Solid-State Batteries. *ACS Energy Lett.* **2021**, 6 (5), 1831–1838.
- (18) Zhou, L.; Minafra, N.; Zeier, W. G.; Nazar, L. F. Innovative Approaches to Li-Argyrodite Solid Electrolytes for All-Solid-State Lithium Batteries. *Acc. Chem. Res.* **2021**, 54 (12), 2717–2728.
- (19) Ji, L.; Gu, M.; Shao, Y.; Li, X.; Engelhard, M. H.; Arey, B. W.; Wang, W.; Nie, Z.; Xiao, J.; Wang, C.; Zhang, J. G.; Liu, J. Controlling SEI formation on SnSb-porous carbon nanofibers for improved Na ion storage. *Adv. Mater.* **2014**, 26 (18), 2901–2908.
- (20) Chen, Y.; Wang, Z.; Li, X.; Yao, X.; Wang, C.; Li, Y.; Xue, W.; Yu, D.; Kim, S. Y.; Yang, F.; Kushima, A.; Zhang, G.; Huang, H.; Wu, N.; Mai, Y.; Goodenough, J. B.; Li, J. Li metal deposition and stripping in a solid-state battery via Coble creep. *Nature* **2020**, 578 (7794), 251–255.
- (21) Zhou, S.; Chen, W.; Shi, J.; Li, G.; Pei, F.; Liu, S.; Ye, W.; Xiao, L.; Wang, M. S.; Wang, D.; Qiao, Yu.; Huang, L.; Xu, G. L.; Liao, H. G.; Chen, J. F.; Amine, K.; Sun, S. G. Efficient diffusion of superdense lithium via atomic channels for dendrite-free lithium–metal batteries. *Energy Environ. Sci.* **2022**, 15 (1), 196–205.
- (22) Yang, G.; Liu, Z.; Weng, S.; Zhang, Q.; Wang, X.; Wang, Z.; Gu, L.; Chen, L. Iron carbide allured lithium metal storage in carbon nanotube cavities. *Energy Storage Mater.* **2021**, 36, 459–465.
- (23) Soto, F. A.; Yan, P.; Englhard, M. H.; Marzouk, A.; Wang, C.; Xu, G.; Chen, Z.; Amine, K.; Liu, J.; Sprenkle, V. L.; El-Mellouhi, F.; Balbuena, P. B.; Li, X. Tuning the Solid Electrolyte Interphase for Selective Li- and Na-Ion Storage in Hard Carbon. *Adv. Mater.* **2017**, 29 (18), No. 1606860.
- (24) Yan, W.; Mu, Z.; Wang, Z.; Huang, Y.; Wu, D.; Lu, P.; Lu, J.; Xu, J.; Wu, Y.; Ma, T.; Yang, M.; Zhu, X.; Xia, Y.; Shi, S.; Chen, L.; Li, H.; Wu, F. Hard-carbon-stabilized Li–Si anodes for high-performance all-solid-state Li-ion batteries. *Nat. Energy* **2023**, 8 (8), 800–813.
- (25) Lee, Y.-G.; Fujiki, S.; Jung, C.; Suzuki, N.; Yashiro, N.; Omoda, R.; Ko, D. S.; Shiratsuchi, T.; Sugimoto, T.; Ryu, S.; Ku, J. H.; Watanabe, T.; Park, Y.; Aihara, Y.; Im, D.; Han, I. T. High-energy long-cycling all-solid-state lithium metal batteries enabled by silver–carbon composite anodes. *Nat. Energy* **2020**, 5 (4), 299–308.
- (26) Ye, L.; Li, X. A dynamic stability design strategy for lithium metal solid state batteries. *Nature* **2021**, 593 (7858), 218–222.
- (27) Spencer-Jolly, D.; Agarwal, V.; Doerr, C.; Hu, B.; Zhang, S.; Melvin, D. R.; Gao, H.; Gao, X.; Adamson, P.; Magdysyuk, O. V.; Grant, P. S.; House, R. A.; Bruce, P. G. Structural changes in the silver–carbon composite anode interlayer of solid-state batteries. *Joule* **2023**, 7 (3), 503–514.
- (28) Du, P.; Fan, X.; Zhang, B.; Cao, L.; Ren, J.; Ou, X.; Guo, X.; Liu, Q. The lithiophobic-to-lithiophilic transition on the graphite towards ultrafast-charging and long-cycling lithium-ion batteries. *Energy Storage Mater.* **2022**, 50, 648–657.
- (29) Alexander, G. V.; Shi, C.; Neill, J. O.; Wachsman, E. D. Extreme lithium-metal cycling enabled by a mixed ion- and electron-conducting garnet three-dimensional architecture. *Nat. Mater.* **2023**, 22 (9), 1136–1143.
- (30) Maxwell, D. C.; O’Keefe, C. A.; Xu, C.; Grey, C. P. C<sup>13</sup> NMR study of the electronic structure of lithiated graphite. *Phys. Rev. Mater.* **2023**, 7 (6), No. 065402.
- (31) Kuhn, A.; Narayanan, S.; Spencer, L.; Goward, G.; Thangadurai, V.; Wilkening, M. Li self-diffusion in garnet-type Li<sub>7</sub>La<sub>3</sub>Zr<sub>2</sub>O<sub>12</sub> as probed directly by diffusion-induced Li<sup>7</sup> spin-lattice relaxation NMR spectroscopy. *Phys. Rev. B* **2011**, 83 (9), No. 094302.
- (32) Boyaci, I. H.; Genis, H. E.; Guven, B.; Tamer, U.; Alper, N. A novel method for quantification of ethanol and methanol in distilled alcoholic beverages using Raman spectroscopy. *J. Raman Spectrosc.* **2012**, 43 (8), 1171–1176.
- (33) Zhao, Z. W.; Pang, L.; Su, Y.; Liu, T.; Wang, X.; Liu, C.; Wang, J.; Peng, Z. Q. Deciphering CO<sub>2</sub> reduction reaction mechanism in aprotic Li–CO<sub>2</sub> batteries using in-situ vibrational spectroscopy coupled with theoretical calculations. *ACS Energy Lett.* **2022**, 7 (2), 624–631.
- (34) Kanamura, K.; Shiraishi, S.; Takezawa, H.; Takehara, Z. I. XPS Analysis of the Surface of a Carbon Electrode Intercalated by Lithium Ions. *Chem. Mater.* **1997**, 9 (8), 1797–1804.
- (35) Henkelman, G.; Uberuaga, B. P.; Jónsson, H. A climbing image nudged elastic band method for finding saddle points and minimum energy paths. *J. Chem. Phys.* **2000**, 113 (22), 9901–9904.
- (36) Liu, Q.; Li, S.; Wang, S.; Zhang, X.; Zhou, S.; Bai, Y.; Zheng, J.; Lu, X. Kinetically Determined Phase Transition from Stage II (LiC<sub>12</sub>) to Stage I (LiC<sub>6</sub>) in a Graphite Anode for Li-Ion Batteries. *J. Phys. Chem. Lett.* **2018**, 9 (8), 5567–5573.
- (37) Persson, K.; Sethuraman, V. A.; Hardwick, L. J.; Hinuma, Y.; Meng, Y. S.; Ven, A. D.; Srinivasan, S.; Kostecki, R.; Ceder, G. Lithium Diffusion in Graphitic Carbon. *J. Phys. Chem. Lett.* **2010**, 1 (8), 1176–1180.
- (38) Kamaya, N.; Homma, K.; Yamakawa, Y.; Hirayama, M.; Kanno, R.; Yonemura, M.; Kamiyama, T.; Kato, Y.; Hama, S.; Kawamoto, K.; Mitsui, A. A lithium superionic conductor. *Nat. Mater.* **2011**, 10 (9), 682–686.
- (39) Mo, Y.; Ong, S. P.; Ceder, G. First Principles Study of the Li<sub>10</sub>GeP<sub>2</sub>S<sub>12</sub> Lithium Super Ionic Conductor Material. *Chem. Mater.* **2012**, 24 (1), 15–17.
- (40) Huggins, R. A. Simple method to determine electronic and ionic components of the conductivity in mixed conductors a review. *Ionics* **2002**, 8, 300–313.
- (41) Asano, T.; Sakai, A.; Ouchi, S.; Sakaida, M.; Miyazaki, A.; Hasegawa, S. Solid Halide Electrolytes with High Lithium-Ion Conductivity for Application in 4 V Class Bulk-Type All-Solid-State Batteries. *Adv. Mater.* **2018**, 30 (44), No. e1803075.
- (42) Liang, J.; Li, X.; Wang, S.; Adair, K.; Li, W.; Zhao, Y.; Wang, C.; Hu, Y.; Zhang, L.; Zhao, S.; Lu, S.; Huang, H.; Li, R.; Mo, Y.; Sun, X. Site-Occupation-Tuned Superionic Li<sub>x</sub>ScCl<sub>3+x</sub> Halide Solid Electrolytes for All-Solid-State Batteries. *J. Am. Chem. Soc.* **2020**, 142 (15), 7012–7022.
- (43) Yin, Y. C.; Yang, J. T.; Luo, J. D.; Lu, G. X.; Huang, Z.; Wang, J. P.; Li, P.; Li, F.; Wu, Y. C.; Tian, T.; Meng, Y. F.; Mo, H. S.; Song, Y. H.; Yang, J.; Feng, L. Z.; Ma, T.; Wen, W.; Kong, K.; Wang, L. J.; Ju, H. X.; Xiao, Y.; Li, Z.; Tao, X. Y.; Yao, H. B. A LaCl<sub>3</sub>-based lithium superionic conductor compatible with lithium metal. *Nature* **2023**, 616, 77–83.
- (44) Zhao, Y.; Daemen, L. L. Superionic conductivity in lithium-rich anti-perovskites. *J. Am. Chem. Soc.* **2012**, 134 (36), 15042–15047.
- (45) Zhu, L.; Wang, Y.; Chen, J.; Li, W.; Wang, T.; Wu, J.; Han, S.; Xia, Y.; Wu, Y.; Wu, M.; Wang, F.; Zheng, Y.; Peng, L.; Liu, J.; Chen, L.; Tang, W. Enhancing ionic conductivity in solid electrolyte by relocating diffusion ions to under-coordination sites. *Sci. Adv.* **2022**, 8 (11), No. eabj7698.
- (46) Sahu, G.; Lin, Z.; Li, J.; Liu, Z.; Dudney, N.; Liang, C. Air-stable, high-conduction solid electrolytes of arsenic-substituted Li<sub>4</sub>SnS<sub>4</sub>. *Energy Environ. Sci.* **2014**, 7, 1053–1058.
- (47) Seino, Y.; Ota, T.; Takada, K.; Hayashi, A.; Tatsumisago, M. A sulphide lithium super ion conductor is superior to liquid ion conductors for use in rechargeable batteries. *Energy Environ. Sci.* **2014**, 7, 627–631.
- (48) Zhao, Y.; Tao, R.; Fujinami, T. Enhancement of ionic conductivity of PEO-LiTFSI electrolyte upon incorporation of plasticizing lithium borate. *Electrochim. Acta* **2006**, 51 (28), 6451–6455.
- (49) Prakash, P.; Fall, B.; Aguirre, J.; Sonnenberg, L. A.; Chinnam, P.; Chereddy, S.; Dikin, D. A.; Venkatnathan, A.; Wunder, S. L.; Zdilla, M. J. A soft co-crystalline solid electrolyte for lithium-ion batteries. *Nat. Mater.* **2023**, 22, 627–635.
- (50) Li, X.; Liang, J.; Yang, X.; Adair, K.; Wang, C. H.; Zhao, F. P.; Sun, X. L. Progress and perspectives on halide lithium conductors for all-solid-state lithium batteries. *Energy Environ. Sci.* **2020**, 13, 1429–1461.